Hindawi
Advances in Mathematical Physics
Volume 2018, Article ID 4906016, 16 pages
https://doi.org/10.1155/2018/4906016

Research Article

Scaling Laws of Droplet Coalescence: Theory and Numerical Simulation

M. Irshad Khodabocus,[1] **Mathieu Sellier**,[2] **and Volker Nock**[3]

[1]*Department of Mathematics, Faculty of Science, University of Mauritius, Réduit 80837, Mauritius*
[2]*Department of Mechanical Engineering, University of Canterbury, Private Bag 4800, Christchurch 8140, New Zealand*
[3]*Department of Electrical and Computer Engineering, University of Canterbury, Private Bag 4800, Christchurch 8140, New Zealand*

Correspondence should be addressed to M. Irshad Khodabocus; ikhodabo@gmail.com

Received 15 July 2018; Accepted 24 September 2018; Published 18 October 2018

Academic Editor: Luigi C. Berselli

When two Newtonian liquid droplets are brought into contact on a solid substrate, a highly curved meniscus neck is established between the two which transforms the bihemispherically shaped fluid domain to a hemispherically shaped domain. The rate at which such topological transformation, called coalescence phenomenon, evolves results from a competition between the inertial force which resists the transformation, the interfacial force which promotes the rate, and the viscous force which arrests it. Depending on the behaviour of these forces, different scaling laws describing the neck growth can be observed, predicted theoretically, and proved numerically. The twofold objective of the present contribution is to propose a simple theoretical framework which leads to an Ordinary Differential Equation, the solution of which predicts the different scaling laws in various limits, and to validate these theoretical predictions numerically by modelling the phenomenon in the commercial Finite Element software COMSOL Multiphysics.

1. Introduction

When two Newtonian liquid droplets are brought into contact on a solid substrate, a highly curved meniscus bridge is established and thereafter driven by surface tension so as to transform the bulk flow region from bihemispherically shaped at early-time regimes to more hemispherically shaped at late-time regimes. Such topological transformation, involving the merging of two or more sessile droplets into a single one on a solid surface, is called *droplet coalescence phenomenon*.

Physically speaking, the coalescence process consists of three regimes, called the *viscous*, *visco-inertia,* and *inertial coalescence regimes* [1]. In each regime, a range of surprisingly complex behaviours can be observed, so to speak topological changes of the interface [2]. Thus, the subject of droplets coalescence is a fascinating, multifaceted subject of inquiry with many interesting phenomena to learn and discover. Indeed, the subject has intrigued many physicists [3–6] and mathematicians [7, 8].

In actual fact, authors of [9] appear to be the first scientists who have addressed the subject. The authors study the formation of vortex rings by droplets falling into liquids and some allied phenomena. For a miscible droplet falling from not too great a height into its bulk fluid, it is observed that the droplet descends through the bulk fluid as a ring, whereas for the case of an immiscible droplet, [9] observed the droplet to descend through the bulk fluid as a spherical droplet. Thereafter, there have been many attempts on experimental, theoretical, and numerical sides to elucidate the underlying physics governing the dynamics of coalescence.

Authors of [10] have studied the partial coalescence of a water droplet, with radius $R \in [0.02, 1.3]$ mm, with the free-surface of a bulk fluid composed of water-glycerol mixtures experimentally. For cases $R \longrightarrow 0.02$, 1.3 mm, the authors drew attention that the coalescence process is arrested by gravitational and viscous effects and, depending on these two effects, three coalescence regimes were observed, which [10] termed *gravity*, *inertio-capillary,* and *viscous* regimes. Furthermore, the authors argued that the coalescence time

is strongly dependent upon the Bond number $\mathrm{Bo} = 4(\rho_1 - \rho_2)gR^2/\gamma$ and the Ohnesorge number $\mathrm{Oh} = \mu_1/(2(\rho_1 + \rho_2)\gamma R)^{1/2}$, where ρ_1, μ_1, and γ denote the density, dynamic viscosity, and surface tension of the droplet, respectively; ρ_1 and μ_1 denote the properties of its vapour phase surrounding, and g denotes the gravitational acceleration.

Reference [7] addressed the more general case of the coalescence of droplets surrounded by a viscous outer fluid, both analytically and numerically, using asymptotic methods and the integral equation given by [11]. Describing the initial coalescence regime by the Stokes equations, they showed that the three-dimensional solution is asymptotically equivalent to the two-dimensional one reported in the works of [12–16]. When the viscosity of the outer fluid is disregarded, the radius and width of the highly curved meniscus bridge were found to obey the following laws: $r_m \sim (t\gamma/\pi\mu)\ln[t\gamma/(\mu R)]$ and $\Delta \propto r_m^3$, respectively, where t is the time, and properties R, γ, and μ are the radius, surface tension, and viscosity constant of the droplet; when the viscosity of the outer fluid is taken into account, a toroidal bubble of radius $\Delta \propto r_m^{3/2}$ is formed by the outer fluid, and $r_m \sim (t\gamma/4\pi\mu)\ln[t\gamma/(\mu R)]$. Employing the Euler equations in the inertial regime, they showed that $r_m \propto (\gamma R/\rho)^{1/4}t^{1/2}$, where ρ denotes the density of the coalescing droplets. (In the present study, the property $b(\boldsymbol{\pi}; t)$ will stand for r_m; $\boldsymbol{\pi}$ designates the set of property constants upon which it depends.)

The paper of [7] is one classic paper which treats the coalescence of droplets both theoretically and numerically. The method used by [7] is termed *conventional* by [8]. The work of [8] is another classic paper on the subject. They addressed the subject using the conventional method and a different method called *interface formation/disappearance method* and comparing their corresponding results with experimental findings. The authors argued that their proposed model shows better agreement with experimental data than the conventional one.

In the literature, [4] has given a combined theoretical and experimental account of the coalescence of water droplets on a solid substrate surrounded by an atmosphere of nitrogen saturated with water. For small contact angle $\theta < 20^\circ$ and large contact angle $\theta \in (70^\circ, 90^\circ)$, the bidroplet undergoes very fast coalescence. Moreover, the relaxation time characterising the coalescence flow is found to be $t_c \propto R$ (or, according to [4], $t_c = \pi\mu/(3K\gamma)$), and the bulk capillary relaxation time, $t_b = R\mu/\gamma \approx t_c \times 10^{-7}$, where R, γ, and μ are the radius, surface tension, and viscosity constant of the bidroplet system.

From a hydrodynamical viewpoint, [3] found that the time evolution of the characteristic scale $b(\boldsymbol{\pi}; t)$ of that small liquid bridge—where the meniscus of the bidroplet system is highly curved—obeys a time-dependent scaling/power law: $b(\boldsymbol{\pi}; t) \propto t^k$, where $k > 0$. For instance, in the *inertial coalescence regime* it was found that $k \approx 1/2$, whereas in the *viscous coalescence regime* $k \approx 1$. The confirmation of these laws as regards the growth of the property $b(\boldsymbol{\pi}; t)$ in those coalescence regimes was also reported by earlier scientists. Reference [2] addressed the early-time evolution of the highly curved meniscus bridge experimentally. They found that $b(\boldsymbol{\pi}; t) \propto K^{1/4}t^{1/2}$, where K is the inverse of the curvature of the meniscus bridge; by comparison, $K = \gamma R/\rho$ [7].

On increasing the viscosity of the fluid, [17] has shown the linear dependence of $b(\boldsymbol{\pi}; t)$ on time. Reference [18] has studied the influence of the geometrical properties of low viscosity liquid droplets experimentally. For contact angles $\theta < 90^\circ$, they deduced $b(\boldsymbol{\pi}; t) \propto t^{2/3}$, while for $\theta > 90^\circ$ their analysis yielded to $b(\boldsymbol{\pi}; t) \propto t^{1/2}$. Most interestingly, they demonstrated the 1/2 exponent scaling law in the limit that $\theta \longrightarrow 90^\circ$, thereby unifying the coalescence of liquid droplets and freely suspended droplets in the inertial regime. The 2/3 exponent scaling law was also argued by [19] who attributed it to the self-similar description of the shape of inviscid pinchoff of a liquid droplet in a still air.

On the other hand, [20] has considered that the influence of surface tension gradient on droplet coalescence was addressed on a combined experimental and numerical basis. The situation considered by these authors was the coalescence of a droplet deposited on the surface of a miscible liquid reservoir. Their results reveal three distinct coalescence regimes based on the reservoir-to-droplet surface tension ratio $\lambda_\gamma > 0$. For instance, the situation $\lambda_\gamma < 0.42$ results in the ejection of a small daughter droplet from the top of the top of the coalescing droplet. Contrarily, it was only when $\lambda_\gamma \in [0.42, 0.93)$ that total coalescence could be observed.

Reference [21] has addressed the early-time coalescence of viscous droplets on a flat, wettable substrate. The authors have shown in terms of their respective radii R_0, initial heights $h_0 \ll R_0$, surface tensions $\gamma > 0$, and dynamics viscosities $\mu > 0$ that $b(\boldsymbol{\pi}; t) \approx (\gamma h_0^3/\mu R_0^2)^{1/2}\sqrt{t}$, which led them to conclude that the evolution of $b(\boldsymbol{\pi}; t)$ is highly sensible to the geometrical properties of the liquid droplets. Reference [22] considered the coalescence of air bubbles and salt water droplets systems in silicone oils experimentally. The proportionality constant and the α-exponent of the scaling law $b(\boldsymbol{\pi}; t) \propto t^\alpha$ are analysed; the authors argued that the evolution of $b(\boldsymbol{\pi}; t)$ is independent of the viscosity of its outer fluid, changing only the proportionality constant by a factor roughly equal to 1.5 and leaving the α-exponent unaffected.

The above references reveal extensive studies of the characters of the property $b(\boldsymbol{\pi}; t) = \kappa \cdot t^\alpha$ with respect to some properly/carefully chosen pair of scalar fields (κ, α), paying little attention to the characters of the coalescence flow fields in three-dimensional space and on cutting planes and leaving the simultaneous establishment of these power law regimes from one and only one generic equation untouched. Moreover, should an attempt be made to study a class of physical situations ranging from droplets spreading to self-propulsion and coalescence, the several modelling frameworks proposed by those scientists are inconvenient to employ without reconstructing either the mathematical framework or the numerical framework, though the outcomes of their works are no doubt striking. Thus, on the one hand, we must admit that a b-evolution equation which permits the deduction of those power laws has never been derived and, on the other hand, the models proposed by those authors make it difficult, if not impossible, to display the global characters of the coalescence flow fields as well as to adapt from one physical situation to another.

In this part, we develop a sound framework which upon variations of an interdependent leading parameter permits to

study either the coalescence of two liquid droplets or the spreading of a single droplet on a three-dimensional solid substrate. Taking advantage of the proposed geometrical model, we then establish through theoretical analysis that b-evolution equation and derive from it the power law relationships $b(\boldsymbol{\pi}; t) \propto t^{\alpha}$ ($\alpha = 1/2, 2/3, 1$).

To demonstrate that the proposed model might be adopted with advantage, the $1/2, 2/3, 1$-exponent scaling laws are proved numerically, and the characters of the coalescence flow fields are illustrated in three-dimensional space and on cutting planes.

2. Theory

2.1. Mathematical Formulations. To formulate the problem mathematically, we reason in the following manner. Suppose two liquid droplets $\Omega_1, \Omega_2 \subset \mathbb{R}^3$ coalesce on a solid substrate $\mathcal{S} \subset \mathbb{R}^3$, at some time $t > 0$ they will occupy a *master* domain $\bigcup_{i=1,2} \Omega_i$ satisfying the geometrical condition

$$\operatorname{vol}\left(\bigcup_{i=1,2} \Omega_i\right) \leq \operatorname{vol}(\Omega_1) + \operatorname{vol}(\Omega_2) \quad \text{for all } t \in (0, T). \tag{1}$$

Following [8], equality follows from (1) only when the size of the *interfacial circular sector* centered at the point $\mathbf{x}_s \in \mathcal{S}$ (see Figure 1) is zero, and strict inequality whenever it is nonzero, as is easily understood. In the present work, the domain $\bigcup_{i=1,2} \Omega_i$, which can vary in time, will be termed *coalescence domain*, though the term *bidroplet system* is also attributed to; the set $(0, T)$ (with $0 < T < \infty$) denotes the period of time over which the study is carried out. Mathematically, the coalescence domain is bounded by two disjoint sets called the *interface* $\partial(\bigcup_{i=1,2} \Omega_i)$ and the *footprint* $\bigcup_{i=1,2} \Omega_i \cap \mathcal{S}$ of the coalescence domain. In Figure 1, we illustrate the coalescence of two viscous liquid droplets $\Omega_1, \Omega_2 \subset \mathbb{R}^3$ conditioned by *zero-flux* of momentum, mass and energy across the (free) surface $\partial(\bigcup_{i=1,2} \Omega_i)$ and the (contact) surface $\bigcup_{i=1,2} \Omega_i \cap \mathcal{S}$; the null flux vectors $\boldsymbol{\varphi}_i = \mathbf{0}$ (with $i = 1, 2, s$) stand for those boundary conditions. Figure 2 exposes to view the projection of the coalescence domain in the (y, z)-plane (top) and in the (x, z)-plane (bottom). Points $\mathbf{x}_0, \mathbf{x}_s \in \mathcal{S}$ designate the rear and centroid of the bidroplet system; and, points $\mathbf{x}_1, \mathbf{x}_2 \in \mathcal{S}$ the centroids of its first and second droplets, both taken at the instant of time $t = 0$. Quantities R_1, R_2 (with $R_2 \leq R_1$) are the initial radii of the coalescing droplets, and $b_0 \equiv b(\boldsymbol{\pi}; t = 0)$ the characteristic size at their corresponding points of contact. In particular, it is assumed in Figure 2 that the coalescence domain is initially *bihemispherical*, L units in length in the direction of $\mathbf{e}_y$, with respective radii R_1, R_2 (with $R_2 \leq R_1$, by hypothesis), and satisfying the condition $R_1 + R_2 < L/2$. (We agree that $R_1 + R_2 = L/2$ necessarily implies that $b_0 = 0$ and, $R_1 + R_2 > L/2$ implies that the coalescing droplets have not yet been brought into contact; see Figure 2.)

The dynamic state of the coalescence domain is characterised completely by the following macroscopic vector and scalar fields quantities: the *velocity* $\mathbf{u}(\mathbf{x}, t) = (u_x, u_y, u_z)^T$ and the *pressure* $p(\mathbf{x}, t)$. We draw attention that, the vector field $\mathbf{u}(\mathbf{x}, t)$ describes the coalescence flow within the coalescence domain $\bigcup_{i=1,2} \Omega_i$.

The *governing equations* describing these property variables in $\bigcup_{i=1,2} \Omega_i$ are the following generic momentum and mass transport equations of a divergence-free flow field:

$$\begin{aligned} \partial_t(\rho\mathbf{u}) + \operatorname{div}(\rho\mathbf{u} \otimes \mathbf{u}) + \nabla p &= \rho\mathbf{f}_\gamma + \operatorname{div}\mathbb{S}(\mathbf{u}) \quad \text{in } \bigcup_{i=1,2} \Omega_i \times (0, T); \\ \operatorname{div}(\rho\mathbf{u}) &= 0 \quad \text{in } \bigcup_{i=1,2} \Omega_i \times (0, T). \end{aligned} \tag{2}$$

In the above system of balance laws, the scalar field $p(\mathbf{x}, t)$ denotes the pressures field and the vector field $\mathbf{f}_\gamma(\mathbf{x}, t)$ denotes the density of volume force due to the surface tension. The tensor $\mathbb{S}(\mathbf{u})$ denotes the *incompressible Newtonian viscous stress tensor*, defined as

$$\mathbb{S}(\mathbf{u}) = \mu\left\{\operatorname{grad}\mathbf{u} + (\operatorname{grad}\mathbf{u})^T\right\} \quad \text{in } \bigcup_{i=1,2} \Omega_i \times (0, T). \tag{3}$$

In (2), the property constants $\rho, \mu > 0$ are, respectively, the *density* and *dynamic viscosity* of the mixed fluid occupying the domain $\bigcup_{i=1,2} \Omega_i$. The operator $\otimes$ designates the *tensor product operator*; for given vector field variables $\mathbf{u}, \mathbf{v} \in \mathbb{R}^3$, their tensor product yields to a 3×3 matrix with the following entries: $\mathbf{u} \otimes \mathbf{v} = u_i v_j$ (with $i, j = x, y, z$).

To model the vector field $\mathbf{f}_\gamma(\mathbf{x}, t)$, we employ the interfacial scalar field $\gamma(\mathbf{x}, t)$ into the following alternative expression

$$\begin{aligned} \mathbf{f}_\gamma(\mathbf{x}, t) &= \operatorname{div}\left(\gamma\left(\nabla_s \cdot \mathbf{n}\right)\mathbf{n} - \nabla_s\gamma\right) \quad \text{on } \partial\left(\bigcup_{i=1,2} \Omega_i\right) \times (0, T); \\ \nabla_s(\cdot) &= (\mathbb{I} - \mathbf{n} \otimes \mathbf{n})\nabla(\cdot). \end{aligned} \tag{4}$$

The detailed derivation of (4) is found in [23]. The vector $\mathbf{n}(\mathbf{x}, t) = (n_x, n_y, n_z)^T$ is the unit outer vector normal to $\bigcup_{i=1,2} \Omega_i$ and $\bigcup_{i=1,2} \Omega_i \cap \mathcal{S}$ ($\neq \bigcup_{i=1,2} \Omega_i$, since, $\Omega_i \cap \mathcal{S} \neq \Omega_i$ for $i = 1, 2$), respectively. The operator $\nabla_s(\cdot)$ is the *surface gradient operator* on $\partial(\bigcup_{i=1,2} \Omega_i)$, and the matrix $\mathbb{I}$ stands for the *identity matrix*.

2.2. Boundary and Initial Conditions. At the instant of time $t = 0$ the distributions of the velocity field $\mathbf{u}(\mathbf{x}, t)$, the pressure field $p(\mathbf{x}, t)$ and the chemical concentration $c(\mathbf{x}, t)$ should be supplemented in $\bigcup_{i=1,2} \Omega_i$, and thereafter conditioned on boundaries $\partial(\bigcup_{i=1,2} \Omega_i)$ and $\bigcup_{i=1,2} \Omega_i \cap \mathcal{S}$ for all $t \in (0, T)$. These are discussed in the following two sections.

The dynamic boundary conditions imposed on the interface $\partial(\bigcup_{i=1,2} \Omega_i)$ for the velocity field $\mathbf{u}(\mathbf{x}, t)$ are the Neumann-type conditions

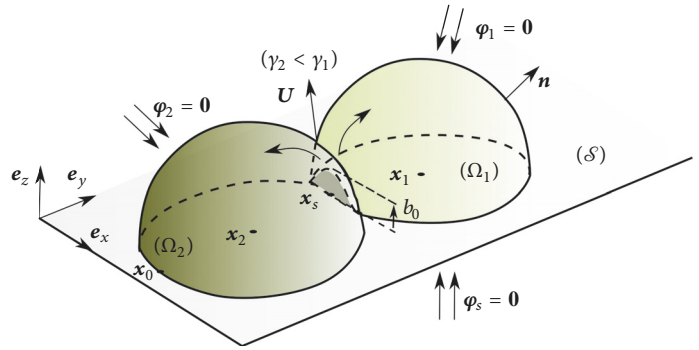

Figure 1: A freehanded illustration of the coalescence of two liquid droplets.

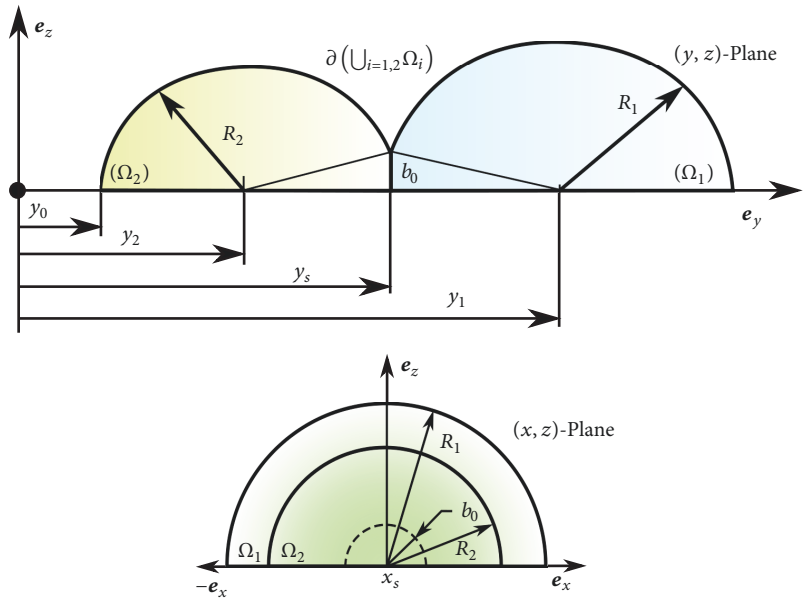

Figure 2: The projection of the coalescence domain in the (y,z)-plane (top) and in the (x,z)-plane (bottom).

$$\begin{aligned}\left(\mathbb{S}(\mathbf{u}) - p\mathbb{I}\right)\mathbf{n} &= \left(-p_{\text{ext}}\mathbb{I} + \gamma\left(\nabla_s \cdot \mathbf{n}\right)\mathbb{I}\right)\mathbf{n} \\ &\quad \text{on } \partial\left(\bigcup_{i=1,2}\Omega_i\right)\times(0,T), \\ \left(\mathbb{S}(\mathbf{u}) - p\mathbb{I}\right)\mathbf{t} &= \left|\nabla_s\gamma\right| \quad \text{on } \partial\left(\bigcup_{i=1,2}\Omega_i\right)\times(0,T).\end{aligned} \tag{5}$$

In the above conditions, the property $p_{\text{ext}} > 0$ designates the *external pressure* applied on the interface $\partial(\Omega_1 \cup \Omega_2)$; $\gamma(\nabla_s \cdot \mathbf{n})$ is the force per unit area due to local curvature of that interface. The term on the right-hand side of the second equation designates the tangential stress associated with gradients in the surface tension coefficient. The proper boundary conditions to be considered on the contact surface $\bigcup_{i=1,2}\Omega_i \cap \mathcal{S}$ are now discussed. At some time $t > 0$ thereafter, the footprint of the coalescence domain $\bigcup_{i=1,2}\Omega_i$ is expected to deform from a *bidisc* shaped domain to a *monodisc* shaped domain. Therefore, a wetted wall boundary condition is considered, the *solid-fluid boundary conditions*. Thus, if the scalar quantity $\beta > 0$ designates the *Navier-slip* coefficient [24], considering the *Navier-slip-with-friction boundary condition* yields

$$\begin{aligned}\left(\mathbb{S}(\mathbf{u})\,\mathbf{n} + \beta\mathbf{u}\right)\cdot\mathbf{t} = 0 \quad &\text{on } \bigcup_{i=1,2}\Omega_i \cap \mathcal{S}\times(0,T), \\ \mathbf{u}\cdot\mathbf{n} = 0 \quad &\text{on } \bigcup_{i=1,2}\Omega_i \cap \mathcal{S}\times(0,T).\end{aligned} \tag{6}$$

In (5), (6), the vector $\mathbf{t}(\mathbf{x},t) = (t_x, t_y, t_z)^T$ designates the tangent vectors to boundaries $\partial(\bigcup_{i=1,2}\Omega_i)$ and $\bigcup_{i=1,2}\Omega_i \cap \mathcal{S}$. The following initial condition is imposed on the vector field $\mathbf{u}(\mathbf{x},t)$ at $t = 0$:

$$\mathbf{u}(\mathbf{x},t) = \mathbf{u}_0(\mathbf{x}) \quad \text{in } \bigcup_{i=1,2}\Omega_i \times \{0\}, \tag{7}$$

The momentum and mass transport equations along with the foregoing set of boundary and initial conditions are solved using the COMSOL Moving Mesh Interface, discussed in what follows.

2.3. Moving Coalescence Domain Explained. At this stage, we have beforehand the mathematical framework and its respective domain of definition. Bearing in mind that the bulk motion of the coalescence domain results from topological changes of its interface from one instant of time to another, to adapt the mathematical descriptions with the movement of the coalescence domain $\bigcup_{i=1,2}\Omega_i$ we employ the *moving mesh method*, which we shall now throw some light upon. For more details, see the works of [23, 25, 26].

Let the interface $\partial(\bigcup_{i=1,2}\Omega_i)$ of the coalescence domain designates a *material point-set* consisting of material points $\mathbf{X} = (X, Y, Z)^T$ at the instant of time $t = 0$. Under this condition, let this coalescence domain at some time $t \geq 0$ be described as a *spatial point-set* consisting of points $\mathbf{x} = (x, y, z)^T$. On the other hand, the coalescence domain being subjected to smooth deformation from one instant to another, there follows that

$$\mathbf{x} = \mathbf{x}(\mathbf{X}, t), \quad \text{on } \partial\left(\bigcup_{i=1,2}\Omega_i\big\rfloor_{t=0}\right)\times(0,T), \tag{8}$$

where $\mathbf{X} = \mathbf{x}(\mathbf{X}, 0)$. Having these *material* and *spatial* vector fields at hand, to relate the topological changes of the interface to its bounded bulk fluid, it suffices to equate the associated velocities on the said interface. Thus, if the vector field $\mathbf{U}(\mathbf{x}, t) = (U_x, U_y, U_z)^T$ describes the movement of the interface, there results in

$$\mathbf{u}\cdot\mathbf{n} = \mathbf{U}\cdot\mathbf{n}, \quad \text{on } \partial\left(\bigcup_{i=1,2}\Omega_i\right)\times(0,T);\ \mathbf{x} = \mathbf{x}(\mathbf{X}, t). \tag{9}$$

Note that, we write $\partial(\bigcup_{i=1,2}\Omega_i\rfloor_{t=0})$ instead of $\partial(\bigcup_{i=1,2}\Omega_i)$ to arrest attention that the interface is undeformed initially.

3. Numerical Implementation

In this section, the construction of the physical domain $\bigcup_{i=1,2}\Omega_i$, described in the (x, y, z)-space by Figure 1 and in the (y, z)-plane by Figure 2, and the numerical implementation of those equations and conditions, namely, (1) to (9), describing its dynamic state is outlined.

The bidroplet system—that is, the coalescence domain—is built as a three-dimensional bihemispherical computational domain sitting on a (x, y)-plane solid substrate. The solid substrate is defined as a rectangular (x, y)-plane sized $L_i > 0$ units in length in the direction of $\mathbf{e}_i$ (with $i = x, y$). To realise these geometrical constructions, the radii R_1, R_2, and position vectors $\mathbf{x}_k = (x_k, y_k, z_k)^T \in \bigcup_{j=1,2}\Omega_j \cap \mathcal{S}$ (with $k = 1, 2, s$) must be supplied, and are tabulated in Table 1. They are based on the following line of reasoning.

Initially, the bidroplet system is assumed symmetrical with respect to the (y, z)-plane. On the solid substrate, the position vector $\mathbf{x}_s = (0, y_s, 0)^T$ denotes its centroid of the coalescence domain $\bigcup_{i=1,2}\Omega_i$; the position vectors $\mathbf{x}_1 = (0, y_1, 0)^T$, $\mathbf{x}_2 = (0, y_2, 0)^T$ denote the centroids of its first and second droplets, respectively. These descriptions are clearly represented in Figure 2. To stress the dependence of the property $b(\boldsymbol{\pi}; t)$ on those geometrical quantities, we consider the following expressions:

Table 1: Initial and boundary conditions imposed on the coalescence domains $\bigcup_{i=1,2}\Omega_i$. Geometrical properties used to generate the b_0-dependent coalescence domains $\bigcup_{i=1,2}\Omega_i$.

ρ	μ	γ	p_{ext}	$\mathbf{u}_0(\mathbf{x})$
[g·cm^{-3}]	[Pa·s]	[N·m^{-1}]	[Pa]	[m·s^{-1}]
1.3	1.4	6×10^{-2}	1.0	$(0,0,0)^T$
$L_x = 2L_y$	$R_1 = R_2$	$\mathbf{x}_1$	$\mathbf{x}_2$	$\mathbf{x}_s$
[mm]	[mm]	[mm]	[mm]	[mm]
10	1.0	$(6,5,0)^T$	$(4,5,0)^T$	$(5,5,0)^T$

$$b(\boldsymbol{\pi}; t) = b_0 = \left(R_i^2 - \left|y_i - y_s\right|^2\right)^{1/2} \quad \text{at } t = 0, \tag{10}$$

where $i = 1, 2$. Furthermore, to stress that the property $b_0 > 0$ is a relatively small quantity initially, we impose the condition $b_0 \ll \min(R_1, R_2)$; in regard to the freehand sketches of Figure 2, this means that $b_0 \ll R_2 \leq R_1$. We note that $b(\boldsymbol{\pi}; t) \geq b_0$ for all $t \geq 0$; thus the coalescence phenomenon is a *relative* process, since it is studied through the evolution of the relative property $b(\boldsymbol{\pi}; t) - b_0$. Consequently, the expansion rate at that region where the curvature is very large is very dependent upon the magnitude of $b_0 > 0$. Clearly, the smaller be the size of the property b_0, the higher be the curvature at the common point of contact of two droplets, and, consequently, the faster be the coalescence rate at early-time.

Topologically, the case for which $b_0 = 0$ prescribes a *one-point interface*, while for the other cases for which $b_0 \neq 0$, all prescribe *infinitely many-points interface*. Since those interfaces disappear for all $t \in (0, T)$, the first case might well be termed the *one-point model* and the other three cases *infinitely many-points model*.

Granted the above descriptions, the following set of equations is implemented: the COMSOL *Laminar Two-Phase Flow Moving Mesh* equations set, having appropriate interfaces of their initial and boundary conditions. This model, as its name implies, is used to describe the spatiotemporal descriptions of the variable field function $\mathbf{u}(\mathbf{x}, t)$. To adapt the COMSOL **u**-equation model with the physical situation under consideration, the COMSOL default model in question is expanded so as to suit the **u**-set of initial and boundary conditions given in earlier (theoretical) sections. The values attributed to those conditions are reported in Table 1.

A series of CFD experiments are ran on this ground and their results are presented in what follows.

4. Results and Discussion

The results to which the proposed model led on a combined theoretical and numerical basis are discussed here.

4.1. Preliminaries. The highly curved meniscus is a fundamental entity. On the grounds of earlier works [3, 18, 19, 21, 27], it can be characterised as follows. By hypothesis, let the d-dimensional sequence $\boldsymbol{\pi} = (\pi_1, \ldots, \pi_d)$ denotes the property-set of $d \geq 1$ positive property constants, upon which rests the character of the coalescence dynamics. Further, let $\psi_\alpha(\boldsymbol{\pi})$ be

a $\boldsymbol{\pi}$-dependent property, where the subscript α stands for the associated α-exponent law. Then, following earlier works one can postulate the following expression:

$$b(\boldsymbol{\pi}, t) = \psi_\alpha(\boldsymbol{\pi}) \cdot t^\alpha, \quad \text{for } t \in (0, \mathrm{T}), \text{ where } \alpha > 0. \tag{11}$$

Given L, T the fundamental units of length and time, the dimensional unit of the property $\psi_\alpha(\boldsymbol{\pi})$ is deduced as follows: We observe that $[\partial_t b] = [\mathrm{L} \cdot \mathrm{T}^{-1}]$, therefore, $[\psi_\alpha] = [\mathrm{L} \cdot \mathrm{T}^{-\alpha}]$, where $\alpha > 0$. Moreover, if by properties b_0, Ψ_{ref}, $\tau_{\mathrm{ref}} > 0$ are meant the characteristic scaling of the scalar fields $b(\boldsymbol{\pi}; t)$, $\psi(\boldsymbol{\pi})$, t, the dimensionless form of (11) reads: $b(\boldsymbol{\pi}; t) = t^\alpha$, where $\mathrm{Ord}(b_0) \sim \Psi_{\mathrm{ref}} \cdot \tau_{\mathrm{ref}}^\alpha$ for some $\alpha > 0$, meaning that the law is independent of the working Newtonian fluids. Consequently, sufficient is that our CFD framework is capable of proving coalescence laws. These statements motivate us to study the coalescence of the bihemispherically shaped droplet system.

5. The Laws of $b(\boldsymbol{\pi};t)$ Predicted Theoretically

Granted the proposed three-dimensional coalescence domain (see Figure 1), and the accompanying two-dimensional geometrical model (see Figure 2) wherein are reflected its geometrical properties in the (x, z)-plane and in the (y, z)-plane, one can predict the time evolution of the property $b(\boldsymbol{\pi}; t)$ in the power law regimes. In the present section, the theoretical prediction of the property $b(\boldsymbol{\pi}; t)$ in those regimes is undertaken. Let it be given $\epsilon \ll 1$, $b_0 > 0$, and $\mathbf{x}_s = (x_s, y_s, z_s)^T \in \bigcup_{i=1,2} \Omega_i \cap \mathcal{S}$, and consider the elementary domain defined by

$$\begin{aligned} \mathscr{B}_\epsilon^0(\mathbf{x}_s) = \{(x, y, z) : \ & |y - y_s| \le \epsilon, \ (x - x_s) \\ & + (z - z_s) \le b_0\}, \end{aligned} \tag{12}$$

with boundary $\partial\mathscr{B}_\epsilon^0(\mathbf{x}_s)$, at the instant of time $t = 0$ (see Figure 3 for geometrical insight). Note that, the elementary domain $\mathscr{B}_\epsilon^0(\mathbf{x}_s) \subset \bigcup_{i=1,2} \Omega_i$ may be conceived of as a 180 degree sector of ϵ-order thick aligned with the (x, z)-plane, and having its footprint centered at the point $\mathbf{x}_s$. The region $\mathscr{B}_\epsilon^0(\mathbf{x}_s)$ is characterised geometrically by the following length and width at time $t = 0$: $\mathrm{leng}(\partial\mathscr{B}_\epsilon^0) = \pi b_0$, $\mathrm{wid}(\partial\mathscr{B}_\epsilon^0) = \epsilon$. Following [7], the coalescence flow is driven by the time evolution of $\partial\mathscr{B}_\epsilon^0(\mathbf{x}_s)$. One can therefore postulate that

$$\begin{aligned} \mathrm{Ord}\left(\left|\mathbf{e}_y \cdot \mathbf{u}(\mathbf{x}_l, t)\right|\right) \sim \mathrm{Ord}\left(\left|\mathbf{e}_y \cdot \mathbf{u}(\mathbf{x}_r, t)\right|\right) \\ \text{at } \mathbf{x}_l, \mathbf{x}_r \in \partial\mathscr{B}_\epsilon^0; \ t \in (0, T). \end{aligned} \tag{13}$$

The placement of the velocity vector fields $\mathbf{u}(\mathbf{x}_r, t)$, $\mathbf{u}(\mathbf{x}_l, t)$ is illustrated in Figure 3. The coalescence dynamics being dominated radially, consequently, the radial component of the equation of motion describing the evolution of the region $\mathscr{B}_\epsilon^0(\mathbf{x}_s)$—from the standpoint of Eulerian description—might at some time $t > 0$ be written in the form

$$\kappa_1 \partial_t^2 b + \frac{\kappa_2}{b^2} \partial_t b + \kappa_3 \partial_b \left(\frac{\gamma}{b}\right) = 0 \quad \text{for } t \in (0, \mathrm{T}). \tag{14}$$

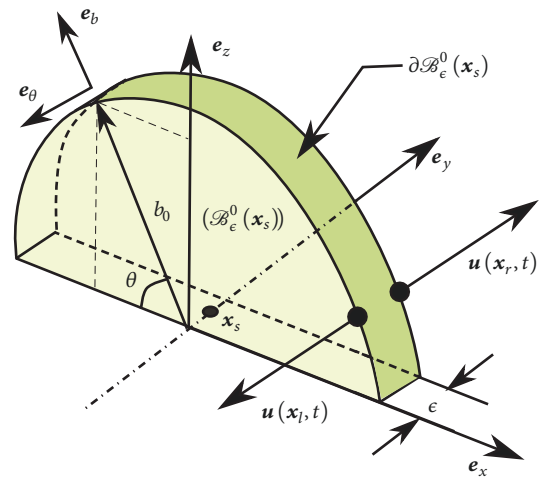

Figure 3: A freehanded sketch of the elementary domain $\mathscr{B}_\epsilon^0(\mathbf{x}_s)$ in $\mathbb{R}^3$.

The establishment of (14) is based on these chains of reasoning. In earlier sections, the standard basis $\{\mathbf{e}_i : i = x, y, z\}$ was used. Here, use of the cylindrical basis $\{\mathbf{e}_\alpha : \alpha = b, \theta, z\}$ will be made to prove (14). Thus, every point $\mathbf{x} = (x, y, z)^T \in \mathscr{B}_\epsilon^0(\mathbf{x}_s)$ on the basis $\{\mathbf{e}_i : i = x, y, z\}$ can be represented by $\mathbf{x} = (b, \theta, y)^T \in \mathscr{B}_\epsilon^0(\mathbf{x}_s)$ on the basis $\{\mathbf{e}_\alpha : \alpha = b, \theta, z\}$. For $t \in (0, T)$, it is postulated that the rate of change of linear momentum equates the differences of capillary and viscous forces across boundary $\partial\mathscr{B}_\epsilon^0(\mathbf{x}_0)$, *i.e.*,

$$\text{Rate of Change of Momentum} = \sum_{\alpha=\mathrm{cap,visc}} \mathbf{f}_\alpha. \tag{15}$$

With this view in mind, one then reasons as follows: The curve traced by a (x, z)-plane $\Pi_{xz}(\mathbf{x}_s)$ cutting the boundary $\partial\mathscr{B}_\epsilon^0(\mathbf{x}_0)$ is described by an equation of the form

$$z(x) = z_s + \left(b^2 - |x - x_s|^2\right)^{1/2} \quad \text{on } \partial\mathscr{B}_\epsilon^0 \cap \Pi_{xz}. \tag{16}$$

Consequently, the curvature of that curve yields

$$\mathrm{curv}\left(\partial\mathscr{B}_\epsilon^0(\mathbf{x}_0)\right) = \frac{\left|\partial_x^2 z(x)\right|}{\left(1 + |\partial_x z(x)|^2\right)^{3/2}} = \frac{1}{b}. \tag{17}$$

On the other hand, an ϵ-volume of $\mathscr{B}_\epsilon^0(\mathbf{x}_0)$ and an ϵ-surface of $\partial\mathscr{B}_\epsilon^0(\mathbf{x}_0)$ gives:

$$\begin{aligned} \mathrm{vol}_\epsilon\left(\mathscr{B}_\epsilon^0(\mathbf{x}_0)\right) &= \epsilon \cdot b \cdot \delta b \cdot \delta\theta \text{ and} \\ \mathrm{surf}_\epsilon\left(\partial\mathscr{B}_\epsilon^0(\mathbf{x}_0)\right) &= \epsilon \cdot b \cdot \delta\theta, \end{aligned} \tag{18}$$

respectively. Note in passing that the plane $\Pi_{xz}(\mathbf{x}_s)$ and $\Pi_{xz}(\mathbf{x}_s)$ are clearly illustrated in Figure 4. Bearing in mind that the property b is a $(\boldsymbol{\pi}; t)$-dependent scalar field, the rate of change of the linear momentum of $\mathrm{vol}_\epsilon(\mathscr{B}_\epsilon^0)$ along $\mathbf{e}_b$, $\boldsymbol{\omega}(\mathscr{B}_\epsilon^0)$ say, then results in

$$\boldsymbol{\omega}\left(\mathscr{B}_\epsilon^0\right) = \rho\partial_t^2 b \cdot \mathrm{vol}_\epsilon\left(\mathscr{B}_\epsilon^0\right)\mathbf{e}_b. \tag{19}$$

The capillary force difference sustained across the interface $\partial\mathscr{B}_\epsilon^0(\mathbf{x}_0)$ is given by

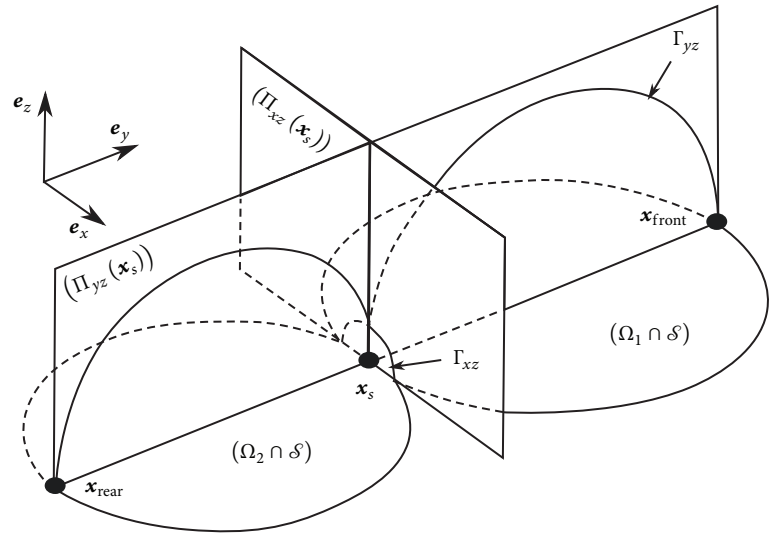

FIGURE 4: Illustration of the planes $\Pi_{\alpha z}(\mathbf{x}_s)$, the corresponding boundary curves $\Gamma_{\alpha z}$ (with $\alpha = x, y$), and the location of the points $\mathbf{x}_{\text{rear}}$, $\mathbf{x}_s$, $\mathbf{x}_{\text{front}} \in \bigcup_{i=1,2}(\Omega_i \cap \mathcal{S})$.

$$\begin{aligned}\delta \mathbf{f}_{\text{cap}}\left(\partial \mathscr{B}_\epsilon^0\right) &= -\delta p \cdot \text{surf}_\epsilon\left(\partial \mathscr{B}_\epsilon^0\right)\mathbf{e}_b \\ &= -\partial_b\left(2\gamma \cdot \text{curv}\left(\partial \mathscr{B}_\epsilon^0\right)\right) \cdot \text{vol}_\epsilon\left(\mathscr{B}_\epsilon^0\right)\mathbf{e}_b \\ &= -\partial_b\left(\frac{2\gamma}{b}\right) \cdot \text{vol}_\epsilon\left(\mathscr{B}_\epsilon^0\right)\mathbf{e}_b.\end{aligned} \tag{20}$$

That due to viscous force is given by

$$\begin{aligned}\delta \mathbf{f}_{\text{visc}}\left(\partial \mathscr{B}_\epsilon^0\right) &= \sum_{i=b,\theta,y}\left\{-\mathbb{S}_{bi}(\mathbf{u}) \cdot \text{surf}_\epsilon\left(\partial \mathscr{B}_\epsilon^0\right)\Big|_b\right. \\ &\quad \left. + \mathbb{S}_{bi}(\mathbf{u}) \cdot \text{surf}_\epsilon\left(\partial \mathscr{B}_\epsilon^0\right)\Big|_{b+\delta b}\right\}\mathbf{e}_b. \\ &= \sum_{i=b,\theta,y} \partial_b\left(b\mathbb{S}_{bi}(\mathbf{u})\right) \cdot \text{vol}_\epsilon\left(\mathscr{B}_\epsilon^0\right)\mathbf{e}_b\end{aligned} \tag{21}$$

In (21), the tensor $\mathbb{S}(\mathbf{u}) = (\mathbb{S}_{ij}(\mathbf{u}))_{i,j=b,\theta,y}$, with $\mathbf{u}$-dependent entries $\mathbb{S}_{ij}(\mathbf{u})$, where i is the row index and j the column index, stands for the viscous stress tensor. Substituting (19) through (21) into (15) yields

$$\rho \partial_t^2 b + \partial_b\left(\frac{2\gamma}{b}\right) - \sum_{i=b,\theta,y} \partial_b\left(b\mathbb{S}_{bi}(\mathbf{u})\right) = 0. \tag{22}$$

For points $\mathbf{x} = (b, \theta, y)^T \in \partial \mathscr{B}_\epsilon^0(\mathbf{x}_0)$, it is asserted that $\mathbf{u} = (u_b, u_\theta, u_y)^T \sim \partial_t b(1, \epsilon, \epsilon)^T$ on the basis of postulate (13), yielding

$$\begin{aligned}&\sum_{i=b,\theta,y} \partial_b\left(b\mathbb{S}_{bi}(\mathbf{u})\right) \\ &= \mu\left(\frac{1}{b}\partial_b\left(\partial_b u_b\right) + \frac{1}{b^2}\partial_\theta^2 u_b + \partial_y^2 u_b - \frac{u_b}{b^2} - \frac{2}{b^2}\partial_\theta u_\theta\right) \\ &\sim -\frac{\mu}{b^2}\partial_t b,\end{aligned} \tag{23}$$

$$\text{since } \mathbf{u} = \left(u_r, u_\theta, u_y\right)^T \sim \partial_t b\,(1, \epsilon, \epsilon)^T.$$

Approximating the last term of (22) by (23) and then setting the triple $(\kappa_1, \kappa_2, \kappa_3) = (\rho, \mu, 2)$, (14) follows. It is to be noted here that $(\kappa_i)_{i=1}^3$ is a $\boldsymbol{\pi}$-dependent sequence because of the dependence of κ_1 on ρ, and κ_2 on μ, as is easily understood. One is now well prepared to discuss the so-called α-exponent laws, α reals.

Granted $b(\boldsymbol{\pi}; t) = \psi(\boldsymbol{\pi}) \cdot t^\alpha$, after its substitution into (14), one arrives at the following algebraic expression:

$$\begin{aligned}&\alpha(\alpha - 1)\kappa_1\left|\psi(\boldsymbol{\pi})\right| t^{\alpha-2} + \frac{\alpha\kappa_2}{\left|\psi(\boldsymbol{\pi})\right|} t^{-\alpha-1} - \frac{\kappa_3\gamma}{\left|\psi(\boldsymbol{\pi})\right|^2} t^{-2\alpha} \\ &\quad = 0.\end{aligned} \tag{24}$$

For that matter of analytical inquiries, set

$$\begin{aligned}\Phi_1(\boldsymbol{\pi}; t) &= \alpha(\alpha - 1)\kappa_1\left|\psi(\boldsymbol{\pi})\right| t^{\alpha-2}, \\ \Phi_2(\boldsymbol{\pi}; t) &= \frac{\alpha\kappa_2}{\left|\psi(\boldsymbol{\pi})\right|} t^{-\alpha-1}, \\ \Phi_3(\boldsymbol{\pi}; t) &= -\frac{\kappa_3\gamma}{\left|\psi(\boldsymbol{\pi})\right|^2} t^{-2\alpha} \\ &\qquad \text{for given } \boldsymbol{\pi}, \text{ and } (\kappa_i)_{i=1}^3,\ t \in (0, T),\end{aligned} \tag{25}$$

respectively. Mathematically, it is proposed to predict the power law behaviour of the property $b(\boldsymbol{\pi}; t)$ based upon the magnitudes of $(\Phi_i)_{i=1}^3$. Since, (24) is a three-term equation, the predictions are argued on three possible pairwise terms.

5.1. Case 1. Suppose that $\text{Ord}(\Phi_1) \sim \text{Ord}(\Phi_2)$, and $\text{Ord}(\Phi_3) \ll 1$. The latter may then be neglected. Thus, for every fixed set of property constants, the following conditions must be fulfilled, namely, $\alpha - 2 = -\alpha - 1$. The law describing this situation therefore writes

$$b(\boldsymbol{\pi}; t) = \psi(\boldsymbol{\pi}) \cdot t^{1/2} \quad \text{for } t \in (0, T). \tag{26}$$

5.2. Case 2. Let it be assumed that $\mathrm{Ord}(\Phi_1) \sim \mathrm{Ord}(\Phi_3)$, and $\mathrm{Ord}(\Phi_2) \ll 1$, respectively. Then, analogous to the above statements, one obtains $\alpha - 2 = -2\alpha$. Thus, $b(\boldsymbol{\pi}; t)$ is in this case of the form

$$b(\boldsymbol{\pi}; t) = \psi(\boldsymbol{\pi}) \cdot t^{2/3} \quad \text{for } t \in (0, T). \tag{27}$$

5.3. Case 3. Conceive the orders of magnitudes of $(\Phi_i)_{i=1}^3$ with respect to themselves to be as follows: $\mathrm{Ord}(\Phi_2) \sim \mathrm{Ord}(\Phi_3)$, and $\mathrm{Ord}(\Phi_1) \ll 1$. In this case, one deduces $-\alpha - 1 = -2\alpha$. Consequently, the scaling law describing the time evolution of the property $b(\boldsymbol{\pi}; t)$ writes

$$b(\boldsymbol{\pi}; t) = \psi(\boldsymbol{\pi}) \cdot t \quad \text{for } t \in (0, T). \tag{28}$$

It is to me pointed out that by $\mathrm{Ord}(\Phi_i)$ is meant the order of magnitude of the property Φ_i (with $i = 1, 2, 3$) with respect to time.

For liquid droplets whose viscosities are not high enough, and having contact angles $\theta < 90^\circ$, practical experiments have shown that $b(\boldsymbol{\pi}; t) \propto t^{2/3}$ [18, 19]. Contrarily, for liquids whose viscosities are high enough and having contact angles $\theta \gtrsim 90^\circ$, many authors have established the law $b(\boldsymbol{\pi}; t) \propto t^{1/2}$ [18, 21, 27]. On the other hand, in purely viscous coalescence regime, the law $b(\boldsymbol{\pi}; t) \propto t$ has also been deduced experimentally [3].

In the next section are proved the power law regimes numerically, thereby giving agreement to experimental data.

6. The Laws of $b(\boldsymbol{\pi};t)$ Proved Numerically

Having established the power laws $b(\boldsymbol{\pi}; t) \propto t^{1/2}, t^{2/3}, t$ theoretically, the chief aim of the present section is to validate them numerically. Before doing so, the groundwork necessary for such endeavours is first laid.

Given the triple $\boldsymbol{\pi}$-dependent proportionality constants $(\psi_\alpha(\boldsymbol{\pi}))_{\alpha \in I_\alpha}$, where $I_\alpha = \{1/2, 2/3, 1\}$. Write $b(\boldsymbol{\pi}; t) = \psi_\alpha(\boldsymbol{\pi}) \cdot t^\alpha$ to stress that the prefactor referred to is the one associated with the α-exponent law and, let quantities b_{theo}, b_{num} stand for its theoretical and numerical predictions, respectively. Thus, to express an ϵ-order discrepancy between the theoretical predictions and the simulation results, one can write $|b_{\text{theo}} - b_{\text{num}}| \sim \mathrm{Ord}(\epsilon)$ and to negate the latter one can write $|b_{\text{theo}} - b_{\text{num}}| \neq \mathrm{Ord}(\epsilon)$. The question arises: Which of those α-exponent laws, $\alpha \in I_\alpha$, should be computed first? The answer to this question lies in the following paragraph.

Suppose two droplets Ω_1, Ω_2 having the same size coalesce and time evolves, the bidroplet system $\bigcup_{i=1,2} \Omega_i$ then will experience a *viscous-inertial coalescence regime* which is preceded by a *viscous coalescence regime* and followed by an *inertial coalescence regime*, as is easily understood. This shows the existence of two overlapping regimes. Moreover, if the set $(0, T_\alpha)$ designates the interval of time over which the law $b(\boldsymbol{\pi}; t) = \psi_\alpha(\boldsymbol{\pi}) \cdot t^\alpha$ holds for some $T_\alpha > 0$, $\alpha \in I_\alpha$, then it is clear that the time intervals corresponding to those three coalescence regimes interrelate themselves as follows:

$$(0, T_1) \subset (0, T_{2/3}) \subset (0, T_{1/2}) \subseteq (0, T). \tag{29}$$

These open sets are termed the *coalescence times* of the corresponding α-regimes, $\alpha \in I_\alpha$. For some $\delta T_\alpha > 0$, $\alpha \in I_\alpha$, it may be said that those two overlapping regimes occur over the time intervals

$$\begin{aligned} &(T_1 - \delta T_1, T_1 + \delta T_{2/3}) \text{ and} \\ &(T_{2/3} - \delta T_1, T_{2/3} + \delta T_{1/2}). \end{aligned} \tag{30}$$

In view of the above discussion, it follows, in chronological order, that the establishment of 2/3-exponent law must precede that of the 1-exponent law and follow that of the 1/2-exponent law. Indeed, if one is to express for every $\alpha \in I_\alpha$ the law $b(\boldsymbol{\pi}; t) = \psi_\alpha(\boldsymbol{\pi}) \cdot t^\alpha$ by making use of the open set $(0, T_\alpha)$, the results would resolve into three algebraic expressions of the forms:

$$\begin{aligned} b(\boldsymbol{\pi}; t) &\approx b_0 + \psi_1(\boldsymbol{\pi}) \cdot t \quad \text{for } t \in (0, T_1), \\ b(\boldsymbol{\pi}; t) &\approx b_0 + \psi_1(\boldsymbol{\pi}) \cdot T_1 + \psi_{2/3}(\boldsymbol{\pi}) \cdot t^{2/3} \\ &\qquad \text{for } t \in (T_1, T_{2/3}), \\ b(\boldsymbol{\pi}; t) &\approx b_0 + \psi_1(\boldsymbol{\pi}) \cdot T_1 + \psi_{2/3}(\boldsymbol{\pi}) \cdot T_{2/3}^{2/3} + \psi_{1/2}(\boldsymbol{\pi}) \\ &\qquad \cdot t^{1/2} \quad \text{for } t \in (T_{2/3}, T_{1/2}). \end{aligned} \tag{31}$$

Carrying out the discussion a step further, one can generalise the form of the scalar field $b(\boldsymbol{\pi}; t)$ with respect to $(\boldsymbol{\pi}; t)$. Supposed granted $\boldsymbol{\pi} = (\pi_i)_{i=1}^d$, where $d > 1$, and $\{\psi_\alpha(\boldsymbol{\pi})\}_{\alpha \in I_\alpha}$ a carefully chosen set of $\boldsymbol{\pi}$-dependent proportionality constants, with the further supposition that $I_\alpha \in \mathbb{Q}$, *i.e.*, $I_\alpha - \{1/2, 2/3, 1\} \neq \emptyset$. Then, it is no error to state that the time evolution of $b(\boldsymbol{\pi}; t)$ in the most general case is a series function of the form:

$$b(\boldsymbol{\pi}; t) \approx b_0 + \sum_{0 < \alpha \leq 1} \psi_\alpha(\boldsymbol{\pi}) \cdot t^\alpha \quad \text{for } t \in (0, T). \tag{32}$$

Leaving (32) out of consideration, thought it appears to demonstrate an important law, hence, might be a fairer, if not the fairest, approximation in practice, the following sections are devoted to the establishment of the laws $b(\boldsymbol{\pi}; t) = \psi_\alpha(\boldsymbol{\pi}) \cdot t^\alpha$, where $\alpha \in I_\alpha$.

6.1. The Viscous Regime Law $b(\boldsymbol{\pi}; t) = \psi_1(\boldsymbol{\pi}) \cdot t$. In this section, the numerical proof of the viscous coalescence power law $b(\boldsymbol{\pi}; t) = \psi_1(\boldsymbol{\pi}) \cdot t$ is proved. How the numerical study has been undertaken may be understood through the following lines.

Numerical experiments is first run. The geometrical properties used to construct the computational domain $\bigcup_{i=1,2} \Omega_i$ are those given in Table 1. The physical properties of the working fluid occupying the domain $\bigcup_{i=1,2} \Omega_i$ as well as the initial and boundary conditions imposed on that domain are those tabulated in Table 1. The said power law is then established in the following manner:

$$\begin{aligned} b_i &= b(\boldsymbol{\pi}; t_i), \\ t_i &= t_0 + i \cdot \delta t, \\ &\qquad \text{where } \delta t > 0, \ i \geq 0, \end{aligned} \tag{33}$$

so that the pair of scalar fields $(t_i, b_i)_{i\geq 0}$ generates a sequence of points in the (t, b)-plane. Obviously, the dimensional units are such that $[b] = [\text{mm}]$ and $[t] = [\text{s}]$ (and $[b] = [L \cdot T^{-\alpha}]$, $\alpha \in I_\alpha$). For every $i \in [0, 12]$, $\delta t = 5$ [ms], the numerical value of (t_i, b_i) is extracted. This gives the necessary data required to describe the time evolution of the geometrical property $b(\boldsymbol{\pi}; t) = \psi_1(\boldsymbol{\pi}) \cdot t$. By means of (33), the pairs of scalar fields $(t_i, b_i)_{i\geq 0}$ are collected in the viscous regime. When plotted in the (t, b)-plane, one obtains the graphical result exposed in Figure 5.

In Figure 5, circular markers $\circ$ are used to represent the numerical data, and the solid line the corresponding fitted power law. This power law function is shaped approximately as follows:

$$b(\boldsymbol{\pi}; t) = \psi_1(\boldsymbol{\pi}) \cdot t \approx 0.0087t - 4.9 \times 10^{-6} \quad \text{for } t \in (0, T). \tag{34}$$

From Figure 5, one sees that $|b_{\text{theo}} - b_{\text{num}}| \sim \text{Ord}(\epsilon)$ only for $t \in (0, T_1)$. The critical instant of time at which $|b_{\text{theo}} - b_{\text{num}}| \neq \text{Ord}(\epsilon)$ is observed at $t \approx 0.05$ [s]; thus, approximately $T_1 \approx 0.05$ [s].

6.2. The Viscous-Inertial Regime Law $b(\boldsymbol{\pi}; t) = \psi_{2/3}(\boldsymbol{\pi}) \cdot t^{2/3}$. The *viscous-inertial* coalescence law $b(\boldsymbol{\pi}; t) = \psi_{2/3}(\boldsymbol{\pi}) \cdot t^{2/3}$ is demonstrated numerically in the present section. The procedure is similar to that discussed in the above section, differing only in the upper bound of the time T. That is, to demonstrate numerically the law $b(\boldsymbol{\pi}; t) = \psi_{2/3}(\boldsymbol{\pi}) \cdot t^{2/3}$, the property values exposed in Table 1 are used, and set $T \approx 0.07$ [s] (*i.e.*, $T > T_1$). Furthermore, since knowing the pair of scalar fields $(t_i, b_i)_{i\geq 0}$ yields the desired law in the (t, b)-plane numerically, to settle the 2/3-exponent law one then proceed in likely the same way as in the earlier section (see Section 6.1).

In Figure 6 are graphed the graphical results. Circular markers $\circ$ are used to represent the numerical data, and the solid line the equation corresponding fitted power law. That fitted power law curve is shaped as

$$b(\boldsymbol{\pi}; t) = \psi_{2/3}(\boldsymbol{\pi}) \cdot t^{2/3} \approx 0.0045t^{2/3} \quad \text{for } t \in (0, T). \tag{35}$$

It is understood that $|b_{\text{theo}} - b_{\text{num}}| \sim \text{Ord}(\epsilon)$ only for $t \in (0, T_{2/3})$. The critical instant of time at which $|b_{\text{theo}} - b_{\text{num}}| \neq \text{Ord}(\epsilon)$ occurs at $t \approx 0.06$ [s]; thus, approximately $T_{2/3} \approx 0.06$ [s].

6.3. The Inertial Regime Law $b(\boldsymbol{\pi}; t) = \psi_{1/2}(\boldsymbol{\pi}) \cdot t^{1/2}$. The power law $b(\boldsymbol{\pi}; t) = \psi_{1/2}(\boldsymbol{\pi}) \cdot t^{1/2}$ is here validated numerically. To do so numerical experiments were first run. The geometrical properties, initial and boundary conditions imposed, and the physical properties of the working fluid are those tabulated in Table 1. The said power law is then established in exactly the same way as in the foregoing two sections (see Sections 6.1 and 6.2).

In Figure 7 are exposed to view their graphical results. Circular markers $\circ$ are used to represent the numerical data, and the solid line the corresponding fitted power law. Through numerical experiments, it is believed that the following scalar function—representative of that solid line curve—gives good agreement:

$$b(\boldsymbol{\pi}; t) = \psi_{1/2}(\boldsymbol{\pi}) \cdot t^{1/2} \approx 0.0026t^{0.49} \quad \text{for } t \in (0, T). \tag{36}$$

In regard to (36), it follows that $\psi_{1/2}(\boldsymbol{\pi}) \approx 0.0026$. The power-the law $b(\boldsymbol{\pi}; t) = \psi_{1/2}(\boldsymbol{\pi}) \cdot t^{1/2}$ is thus proved numerically, demonstrated experimentally by [18, 21, 27]. It may be remarked that $|b_{\text{theo}} - b_{\text{num}}| \sim \text{Ord}(\epsilon)$ only for $t \in (0, T_{1/2})$. The critical instant of time at which $|b_{\text{theo}} - b_{\text{num}}| \neq \text{Ord}(\epsilon)$ occurs at $t \approx 0.17$ [s]; thus, approximately $T_{1/2} \approx 0.17$ [s]. The values of the scalar fields $T_i > 0$ $(i = 1/2, 2/3, 1)$ are observed to be roughly equal to these values:

$$\begin{aligned} T_1 &\approx 0.05 \text{ [s]}, \\ T_{2/3} &\approx 0.06 \text{ [s]}, \text{ and} \\ T_{1/2} &\approx 0.17 \text{ [s]}. \end{aligned} \tag{37}$$

Moreover, from (36), (34), (35), one also observes that

$$\text{Ord}\left(\psi_\alpha(\boldsymbol{\pi})\right) \sim 10^{-3} \left[\text{mm}\cdot\text{s}^{-\alpha}\right] \quad \text{for all } \alpha \in I_\alpha. \tag{38}$$

In what follows the $\boldsymbol{\pi}$-dependent sequence $(\psi_\alpha(\boldsymbol{\pi}))_{\alpha\in I_\alpha}$ are analysed.

6.4. Of the Characters of $(\psi_\alpha(\boldsymbol{\pi}))_{\alpha\in I_\alpha}$. When the literature was surveyed, one found no more than two elements of the sequence $(\psi_\alpha(\boldsymbol{\pi}))_{\alpha\in I_\alpha}$ have gained attention, yet their establishment in terms of the property constants involved in the problems they ultimately lie have been correctly settled. With this view in mind, it is proposed to discuss in the present section the characters of $(\psi_\alpha(\boldsymbol{\pi}))_{\alpha\in I_\alpha}$ through analysis.

The analysis commences by relating the leading property associated with the interfacial coalescence hydrodynamics to that associated with the bulk coalescence hydrodynamics, that is, it is proposed to relate $b(\boldsymbol{\pi}; t)$ to $\mathbf{u}(\mathbf{x}, t)$ on Γ_{xz}. It is clear that $b(\boldsymbol{\pi}; t) = \|\mathbf{x} - \mathbf{x}_s\|$, where $\mathbf{x}, \mathbf{x}_s \in \Pi_{xz}(\mathbf{x}_s)$. Therefore, taking its derivative, one obtains

$$\mathbf{u} \cdot (\mathbf{x} - \mathbf{x}_s) = \alpha \left|\psi_\alpha(\boldsymbol{\pi})\right|^2 t^{2\alpha-1} \quad \text{on } \Gamma_{xz} \times (0, T_\alpha), \text{ where } \alpha \in I_\alpha. \tag{39}$$

On the other hand, the leading property constants being ρ, μ, γ_0, b_0, R_1, consequently, $\boldsymbol{\pi} = (\rho, \mu, \gamma_0, b_0, R_1)^T$. Given the characteristic scales $(T_\alpha, X_\alpha, U_\alpha, \Psi_\alpha)_{\alpha\in I_\alpha}$, one rescales the properties appearing in (39) as follows: $t \longmapsto T_\alpha t$, $\mathbf{x} \longmapsto \mathbf{x}_s + X_\alpha(\mathbf{x} - \mathbf{x}_s)$, $\mathbf{u} \longmapsto U_\alpha \mathbf{u}$, and $\psi_\alpha \longmapsto \Psi_\alpha \psi_\alpha$, yielding

$$\text{Ord}\left(\left|\Psi_\alpha(\boldsymbol{\pi})\right|\right) \sim \sqrt{\frac{U_\alpha X_\alpha}{\alpha T_\alpha^{2\alpha-1}}}, \quad \text{where } \alpha \in I_\alpha. \tag{40}$$

It now remains to express the right-hand side of (40) in terms of the property vector $\boldsymbol{\pi} = (\rho, \mu, \gamma_0, b_0, R_1)^T$. To do this, one reasons according to the α-regimes, where $\alpha \in I_\alpha$.

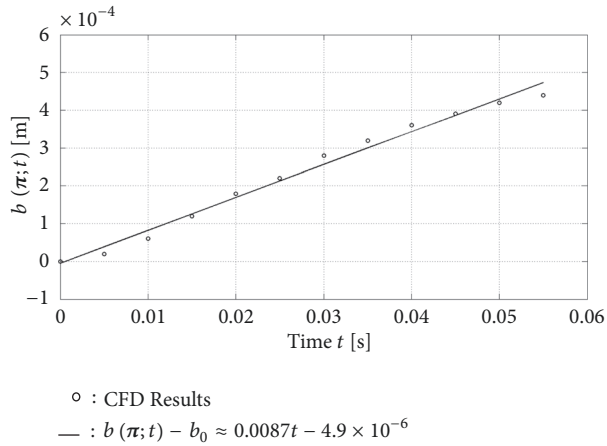

Figure 5: Time evolution of the neck heights $b(\boldsymbol{\pi}; t)$ in the viscous regime. The *circular markers* ∘ indicate the numerical experiment results and the solid line represents the fitted curve.

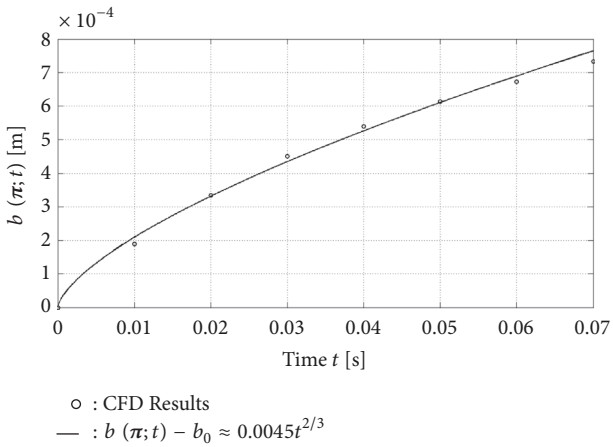

Figure 6: Time evolution of the neck heights $b(\boldsymbol{\pi}; t)$ in the inertial-viscous regime. The *circular markers* ∘ indicate the numerical experiment results and the solid line represents the fitted curve.

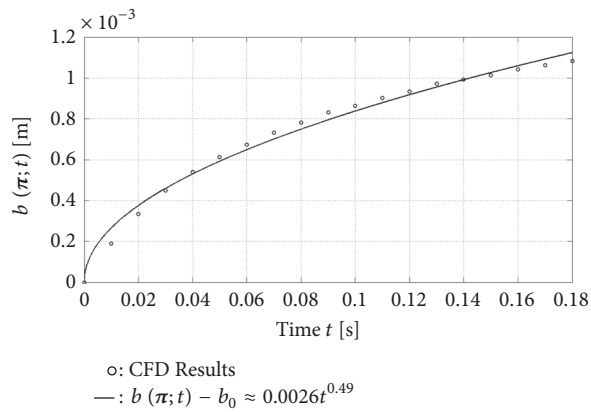

Figure 7: Time evolution of the neck heights $b(\boldsymbol{\pi}; t)$ in the inertial regime. The *circular markers* ∘ indicate the numerical experiment results and the solid line represents the fitted curves.

Analysing the set of properties $(T_\alpha, X_\alpha, U_\alpha)_{\alpha\in I_\alpha}$ in terms of $\boldsymbol{\pi}$, the following orders of magnitude follow:

$$\begin{aligned}
\mathrm{Ord}\,(T_1, T_{2/3}, T_{1/2}) &\sim \left(\frac{\mu b_0}{\gamma_0}, \frac{\mu b_0}{\gamma_0}, \sqrt{\frac{\rho R_1^3}{\gamma_0}}\right),\\
\mathrm{Ord}\,(X_1, X_{2/3}, X_{1/2}) &\sim (b_0, b_0, R_1),\\
\mathrm{Ord}\,(U_1, U_{2/3}, U_{1/2}) &\sim \left(\frac{\gamma_0}{\mu}, \frac{\gamma_0}{\mu}, \sqrt{\frac{\gamma_0}{\rho R_1}}\right).
\end{aligned} \tag{41}$$

These being so, substituting (41) into (40), one finds

$$\begin{aligned}
&\mathrm{Ord}\left(\left|\Psi_1(\boldsymbol{\pi})\right|, \left|\Psi_{2/3}(\boldsymbol{\pi})\right|, \left|\Psi_{1/2}(\boldsymbol{\pi})\right|\right)\\
&\sim \left(\frac{\gamma_0}{\mu}, \sqrt{\frac{3}{2}}\left(\frac{\gamma_0^2 b_0}{\mu^2}\right)^{1/3}, \sqrt{2}\left(\frac{\gamma_0 R_1}{\rho}\right)^{1/4}\right).
\end{aligned} \tag{42}$$

Moreover, inserting the property constants of Table 1 into (42) and, thereafter, dividing each element of $(\psi_\alpha(\boldsymbol{\pi})\rfloor_{\mathrm{theo}})_{\alpha\in I_\alpha}$ by the corresponding element of $(\psi_\alpha(\boldsymbol{\pi})\rfloor_{\mathrm{num}})_{\alpha\in I_\alpha}$, the orders of magnitude of the ratio of $\Psi_\alpha(\boldsymbol{\pi})\rfloor_{\mathrm{theo}}$ to $\Psi_\alpha(\boldsymbol{\pi})\rfloor_{\mathrm{num}}$ yield

$$\mathrm{Ord}\left(\frac{\Psi_\alpha(\boldsymbol{\pi})\rfloor_{\mathrm{theo}}}{\Psi_\alpha(\boldsymbol{\pi})\rfloor_{\mathrm{num}}}\right) \approx 4.5 \sim \mathrm{Ord}\,(1) \quad \text{for all } \alpha \in I_\alpha. \tag{43}$$

In (43), it is understood that quantities $\Psi_\alpha(\boldsymbol{\pi})\rfloor_{\mathrm{theo}}, \Psi_\alpha(\boldsymbol{\pi})\rfloor_{\mathrm{num}}$ stand for the theoretical and numerical estimation, respectively, of the scalar field $\Psi_\alpha(\boldsymbol{\pi})$. Expressing (34), (35) and (36) in terms of (42) gives

$$\begin{aligned}
b(\boldsymbol{\pi}; t) &\sim \frac{\gamma_0}{\mu} t \quad \text{for } t \in (0, T_1),\\
b(\boldsymbol{\pi}; t) &\sim \sqrt{\frac{3}{2}}\left(\frac{\gamma_0^2 b_0}{\mu^2}\right)^{1/3} t^{2/3} \quad \text{for } t \in (0, T_{2/3}),\\
b(\boldsymbol{\pi}; t) &\sim \sqrt{2}\left(\frac{\gamma_0 R_1}{\rho}\right)^{1/4} t^{1/2} \quad \text{for } t \in (0, T_{1/2}).
\end{aligned} \tag{44}$$

Equation (44) at once justifies the reasonableness of the foregoing chains of reasoning and, this completes the discussion of the present section concerning the $(\boldsymbol{\pi}; t)$-dependent evolution of the field $b(\boldsymbol{\pi}; t)$. In the next section, it is proposed to enter upon the discussion of the characters of the curve $\mathbf{u}(\mathbf{x}, t)$ along a carefully chosen one-dimensional boundary.

6.5. Of the Characters of $\mathbf{u}(\mathbf{x}, t)$. If the velocity norm $\|\mathbf{u}\|$ of the interacting droplets systems is plotted on the curved boundary Γ_{yz}, the curve traced by the intersection of the interface $\partial(\Omega_1 \cup \Omega_2)$ with the plane $\Pi_{yz}(\mathbf{x}_s)$, one obtains Figure 8. The placement of arrows on the $\mathbf{u}$ curves of Figure 8 serve merely to indicate the evolution of time evolution of these curves. In Figure 8, the graphs of the velocity norm $\|\mathbf{u}\|$ correspond to the sequence of times $(t_k)_{k=0}^5 = (10k)$ [ms]. The nature of these curves are now explained.

Inspecting Figure 8, one sees that the highly curved meniscus induces an ϵ-order singularity into the coalescence flow in the early-time regime, peaking to magnitudes of the order of $\|\mathbf{u}\| \approx 20$ mm·s^{-1} inside that highly curved meniscus zone (indicated by dashed, vertical lines). It is perhaps because of this striking effect that some authors have characterised such motion as *singular motion* [7, 22].

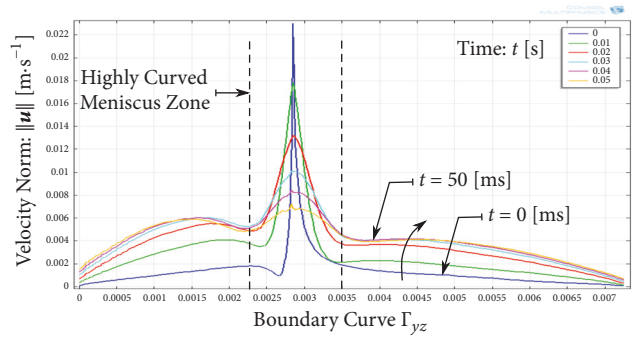

FIGURE 8: Time evolution of the velocity norm $\|\mathbf{u}\|$ of two interacting droplets with radii R_1, R_2 (with $R_2 = R_1$) along the boundary curve Γ_{yz} for the sequence of times $(t_k)_{k=0}^5 = (10k)_{k=0}^5$ [ms].

It is interesting to see the spatiotemporal distributions of the field variable $\mathbf{u}(\mathbf{x}, t)$. This is the purpose of the next section.

7. The Coalescence Flow Fields Illustrated

Having discussed the growth of the time-dependent function $b(\boldsymbol{\pi}; t)$ in the inertial, inertial-viscous and viscous regimes, the evolutions of the vector field function $\mathbf{u}(\mathbf{x}, t)$ with respect to $(\mathbf{x}, t) \in \bigcup_{i=1,2} \Omega_i \times (0, T)$ are now reported. In few words, the present endeavours is an attempt to lay additional stress on the qualitative aspects of the proposed model.

When the coalescence domain $\bigcup_{i=1,2} \Omega_i$ undergoes coalescence phenomenon, as soon as its pair of droplets are brought into contact, a mass movement is started, thereby causing the corresponding droplets to fuse. It is not necessary to go into details; sufficient is to demonstrate that the proposed model is capable of describing the underlying motion phenomena and the latter are exposed in the $3D$ space and on the $2D$ planes $\Pi_{\alpha z}(\mathbf{x}_s)$ (with $\alpha = x, y$).

In Figures 9 and 10, the time evolutions of the velocity norm $\|\mathbf{u}\|$ of the coalescence domain $\bigcup_{i=1,2} \Omega_i$ at times $t =$ 5, 50, 100, 190 [ms] are exposed in the $3D$ space. The corresponding two-dimensional plots of the scalar field $\|\mathbf{u}\|$ are reported, respectively, on the $2D$ planes $\Pi_{\alpha z}(\mathbf{x}_s)$ (with $\alpha = x, y$) given in Figures 11–14, where solid lines stand for the iso-$\|\mathbf{u}\|$ contours.

8. Closing Remarks

In this part, a three-dimensional modelling methodology has been proposed to study droplets coalescence phenomenon. On the whole, the statements arrived at conclusively are:

When, upon variations of geometrical parameters, the footprint $\bigcup_{i=1,2}(\Omega_i \cap \mathcal{S})$ and the free-surface $\partial(\Omega_1 \cup \Omega_2)$ of the bidroplet system $\bigcup_{i=1,2} \Omega_i$ reduce to the footprint $\Omega_2 \cap \mathcal{S}$ and

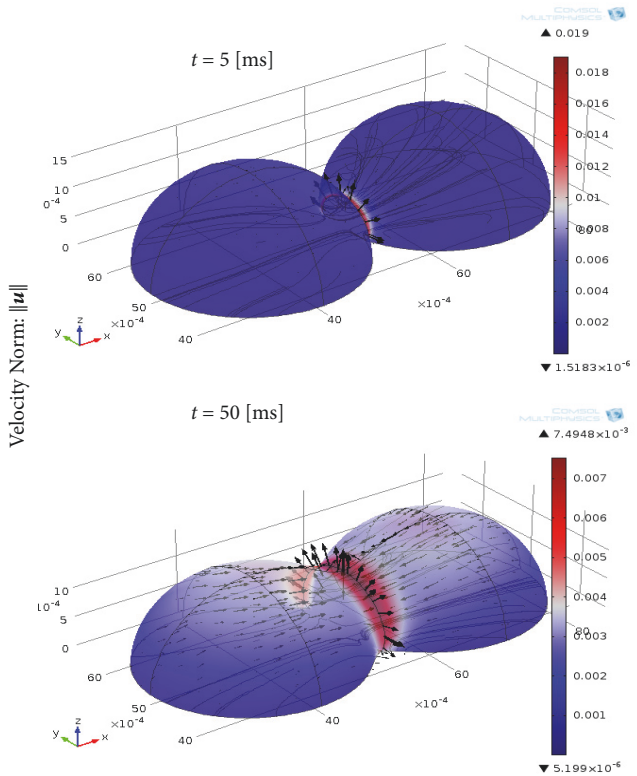

FIGURE 9: Three-dimensional plots of the velocity norm $\|\mathbf{u}\|$ of two interacting droplets of the same radius $R_1 = R_2$ at times $t = 5, 50$ [ms].

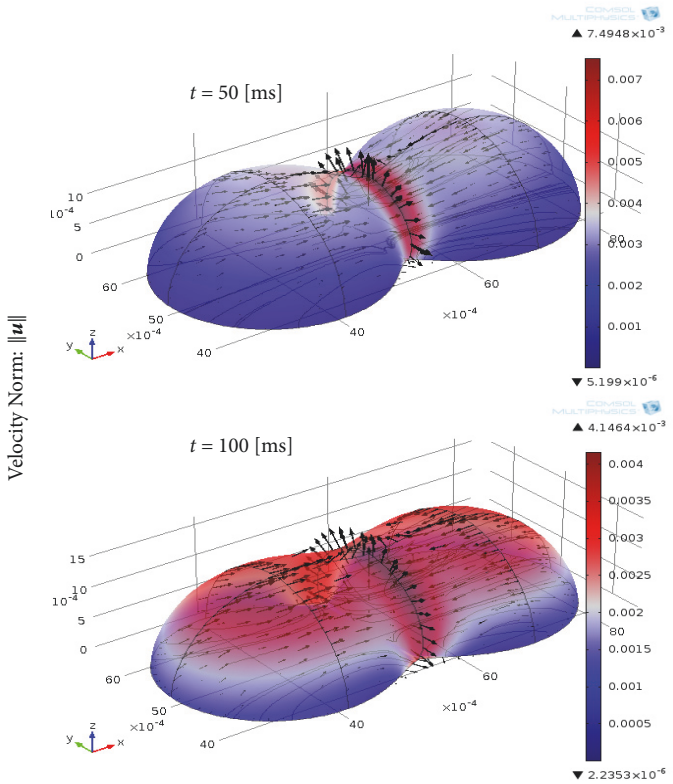

FIGURE 10: Three-dimensional plots of the velocity norm $\|\mathbf{u}\|$ of two interacting droplets of the same radius $R_1 = R_2$ at times $t = 100, 190$ [ms].

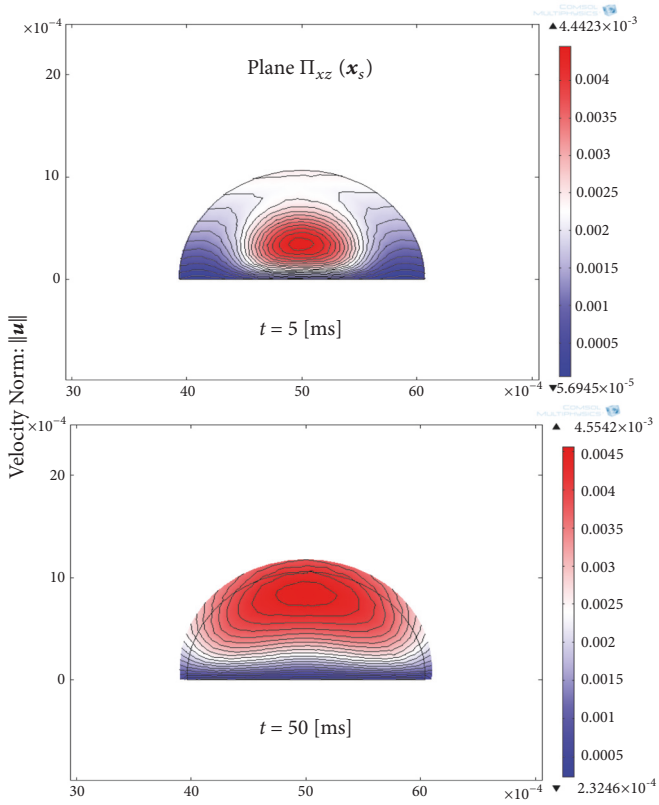

FIGURE 11: Two-dimensional plots of the velocity norm $\|\mathbf{u}\|$ of two interacting droplets of the same radius $R_1 = R_2$ on the plane $\Pi_{xz}(\mathbf{x}_s)$ at times t = 5, 50 [ms]. The solid lines stand for the iso-$\|\mathbf{u}\|$ contours.

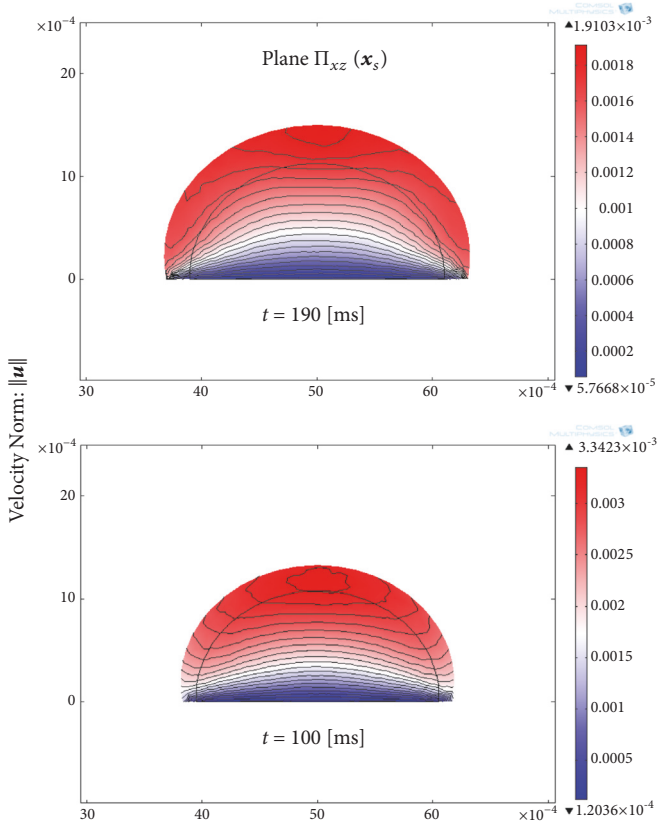

FIGURE 12: Two-dimensional plots of the velocity norm $\|\mathbf{u}\|$ of two interacting droplets of the same radius $R_1 = R_2$ on the plane $\Pi_{xz}(\mathbf{x}_s)$ at times t = 100, 190 [ms]. The solid lines stand for the iso-$\|\mathbf{u}\|$ contours.

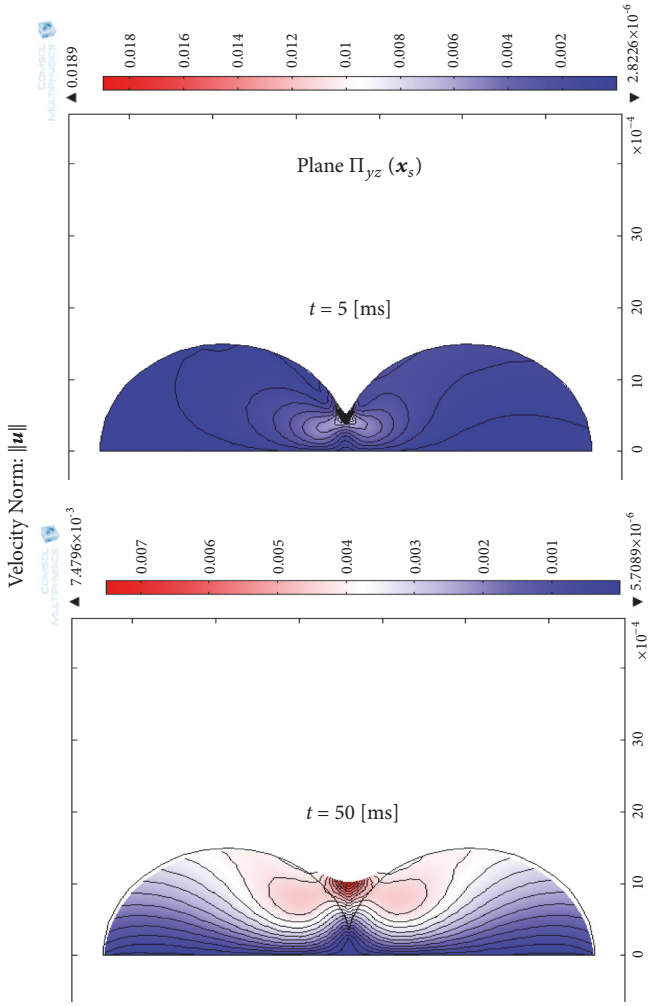

FIGURE 13: Two-dimensional plots of the velocity norm $\|\mathbf{u}\|$ of two interacting droplets of the same radius $R_1 = R_2$ on the plane $\Pi_{xz}(\mathbf{x}_s)$ at times $t = 5, 50$ [ms]. The solid lines stand for the iso-$\|\mathbf{u}\|$ contours.

the free-surface $\partial\Omega_2$, respectively, of a monodroplet system Ω_2, the corresponding boundary conditions are by default adapted into the COMSOL interfaces. As a result, with one numerical model, its property constants can be so arranged so as to compute many physical situations, a task which one would have undertaken had the proposed model been unversatile.

Taking advantage of the geometrical features of the proposed model, it is possible to deduce through theoretical analysis the scaling laws $b(\boldsymbol{\pi}; t) = \psi_\alpha(\boldsymbol{\pi}) \cdot t^\alpha$ (with $\alpha = 1/2$, $2/3$, 1), laws already reported in the (experimental) literature.

Carried out numerical proofs of these laws, $\alpha \approx 1$ is observed in the visco-dominated coalescence flow, $\alpha \approx 2/3$ in the inertia-visco-dominated coalescence flow, and $\alpha \approx 1/2$ in the inertia-dominated coalescence flow.

Through scaling analysis, it is found that the dependence of the sequence of prefactors $(\psi_\alpha(\boldsymbol{\pi}))_{\alpha \in I_\alpha}$ on $\boldsymbol{\pi} = (\rho, \mu, \gamma_0, b_0, R_1)^T$ can be approximated as follows: $\psi_1(\boldsymbol{\pi}) \approx \gamma_0/\mu, \psi_{2/3}(\boldsymbol{\pi}) \approx \sqrt{3/2}(\gamma_0^2 b_0/\mu^2)^{1/3}$ and $\psi_{1/2}(\boldsymbol{\pi}) \approx \sqrt{2}(\gamma_0 R_1/\rho)^{1/4}$.

The flow field variables illustrated by $2D$, $3D$ plots clearly demonstrate that the expected features associated with droplets coalescence phenomenon are well captured by the model.

On the whole, yet the approach in the present analysis has been to present the leading features of the proposed model by considering the coalescence that results under an idealized situation, it is no way contradictory to declare that it can be used to model more complex physical situations. For example, numerical experiments on droplets coalescence phenomenon can be carried out under appropriate CFD conditions to display useful information concerning mixing process driven by Marangoni flow.

Data Availability

The data used to support the findings of this study are available from the corresponding author upon request.

Disclosure

The current address of M. I. Khodabocus and M. Sellier is Mechanical Engineering Department, University of

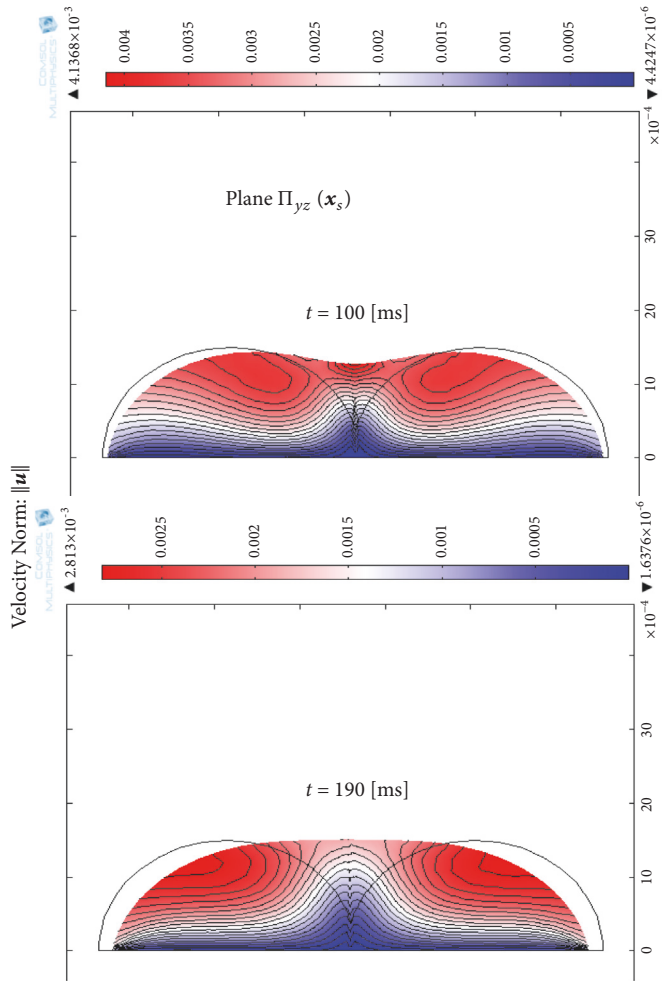

FIGURE 14: Two-dimensional plots of the velocity norm $\|\mathbf{u}\|$ of two interacting droplets of the same radius $R_1 = R_2$ on the plane $\Pi_{xz}(\mathbf{x}_s)$ at times t = 100, 190 [ms]. The solid lines stand for the iso-$\|\mathbf{u}\|$ contours.

Canterbury, Private Bag 4800, Christchurch 8140, New Zealand. The current address of V. Nock is Electrical and Computer Engineering Department, University of Canterbury, Private Bag 4800, Christchurch 8140, New Zealand.

Conflicts of Interest

The authors declare that they have no conflicts of interest.

References

[1] J. D. Paulsen, J. C. Burton, S. R. Nagel, S. Appathurai, M. T. Harris, and O. A. Basaran, "The inexorable resistance of inertia determines the initial regime of drop coalescence," *Proceedings of the National Acadamy of Sciences of the United States of America*, vol. 109, no. 18, pp. 6857–6861, 2012.

[2] M. M. Wu, T. Cubaud, and C.-M. Ho, "Scaling law in liquid drop coalescence driven by surface tension," *Physics of Fluids*, vol. 16, no. 7, pp. L51–L54, 2004.

[3] D. G. Aarts, H. N. Lekkerkerker, H. Guo, G. H. Wegdam, and D. Bonn, "Hydrodynamics of droplet coalescence," *Physical Review Letters*, vol. 95, no. 16, 2005.

[4] C. Andrieu, D. A. Beysens, V. S. Nikolayev, and Y. Pomeau, "Coalescence of sessile drops," *Journal of Fluid Mechanics*, vol. 453, pp. 427–438, 2002.

[5] M. Sellier, V. Nock, and C. Verdier, "Self-propelling, coalescing droplets," *International Journal of Multiphase Flow*, vol. 37, no. 5, pp. 462–468, 2011.

[6] M. Sellier, V. Nock, C. Gaubert, and C. Verdier, "Droplet actuation induced by coalescence: experimental evidences and phenomenological modeling," *The European Physical Journal Special Topics*, vol. 219, no. 1, pp. 131–141, 2013.

[7] J. Eggers, J. R. Lister, and H. A. Stone, "Coalescence of liquid drops," *Journal of Fluid Mechanics*, vol. 401, pp. 293–310, 1999.

[8] J. E. Sprittles and Y. D. Shikhmurzaev, "Coalescence of liquid drops: Different models versus experiment," *Physics of Fluids*, vol. 24, no. 12, 2012.

[9] J. J. Thomson and H. F. Newall, "On the formation of vortex rings by drops falling into liquids, and some allied phenomena," *Proceedings of The Royal Society of London*, vol. 39, no. 239-241, pp. 417–436, 1885.

[10] X. Chen, S. Mandre, and J. J. Feng, "Partial coalescence between a drop and a liquid-liquid interface," *Physics of Fluids*, vol. 18, no. 5, p. 051705, 2006.

[11] J. M. Rallison and A. Acrivos, "A numerical study of the deformation and burst of a viscous drop in an extensional flow," *Journal of Fluid Mechanics*, vol. 89, no. 1, pp. 191–200, 1978.

[12] R. W. Hopper, "Plane Stokes flow driven by capillarity on a free surface," *Journal of Fluid Mechanics*, vol. 213, pp. 349–375, 1990.

[13] R. W. Hopper, "Stokes flow of a cylinder and half-space driven by capillarity," *Journal of Fluid Mechanics*, vol. 243, pp. 171–181, 1992.

[14] R. W. Hopper, "Coalescence of two viscous cylinders by capillarity: Part I, theory," *Journal of the American Ceramic Society*, vol. 76, no. 12, pp. 2947–2952, 1993.

[15] R. W. Hopper, "Coalescence of two viscous cylinders by capillarity: Part II, shape evolution," *Journal of the American Ceramic Society*, vol. 76, no. 12, pp. 2953–2960, 1993.

[16] S. Richardson, "Two-dimensional slow viscous flows with time-dependent free boundaries driven by surface tension," *European Journal of Applied Mathematics*, vol. 3, no. 3, pp. 193–207, 1992.

[17] W. Yao, H. J. Maris, P. Pennington, and G. M. Seidel, "Coalescence of viscous liquid drops," *Physical Review E: Statistical, Nonlinear, and Soft Matter Physics*, vol. 71, no. 1, 2005.

[18] A. Eddi, K. G. Winkels, and J. H. Snoeijer, "Influence of droplet geometry on the coalescence of low viscosity drops," *Physical Review Letters*, vol. 111, no. 14, 2013.

[19] R. F. Day, E. J. Hinch, and J. R. Lister, "Self-similar capillary pinchoff of an inviscid fluid," *Physical Review Letters*, vol. 80, no. 4, pp. 704–707, 1998.

[20] F. Blanchette, L. Messio, and J. W. M. Bush, "The influence of surface tension gradients on drop coalescence," *Physics of Fluids*, vol. 21, no. 7, 2009.

[21] W. D. Ristenpart, P. M. McCalla, R. V. Roy, and H. A. Stone, "Coalescence of spreading droplets on a wettable substrate," *Physical Review Letters*, vol. 97, no. 6, 2006.

[22] J. D. Paulsen, R. Carmigniani, A. Kannan, J. C. Burton, and S. R. Nagel, "Coalescence of bubbles and drops in an outer fluid," *Nature Communications*, vol. 5, pp. 1–7, 2014.

[23] B. Lafaurie, C. Nardone, R. Scardovelli, S. Zaleski, and G. Zanetti, "Modelling merging and fragmentation in multiphase flows with SURFER," *Journal of Computational Physics*, vol. 113, no. 1, pp. 134–147, 1994.

[24] C. L. Navier, "Mémoire sur les Lois Mouvement des Fluides," *Mémoires de l'Académie Royale des Sciences de l'Institut de France*, vol. 6, pp. 389–440, 1823.

[25] J.-F. Gerbeau and T. Lelievre, "Generalized Navier boundary condition and geometric conservation law for surface tension," *Computer Methods Applied Mechanics and Engineering*, vol. 198, no. 5-8, pp. 644–656, 2009.

[26] R. Scardovelli and S. Zaleski, "Direct numerical simulation of freesurface and interfacial flow," *Annual Review of Fluid Mechanics*, vol. 31, no. 1, pp. 567–603, 1999.

[27] L. Duchemin, J. Eggers, and C. Josserand, "Inviscid coalescence of drops," *Journal of Fluid Mechanics*, no. 487, pp. 167–178, 2003.